Seasonal and interannual Variability of the Subtropical South Indian Ocean Sea Surface Salinity Maximum

F. M. Bingham[1], S. K. Brodnitz[1], and A. L. Gordon[2]

[1]University of North Carolina Wilmington, Center for Marine Science.

[2]Lamont Doherty Earth Observatory, Columbia University.

Corresponding author: Frederick M. Bingham (binghamf@uncw.edu)

Key Points:

- We have studied the seasonal and interannual variability in the size and position of the South Indian Ocean sea surface salinity maximum
- The feature moves on a northeast-southwest track, with correlated changes in size
- Variability seems to be associated with changes in gyre-scale flows and wind forcing, not surface freshwater input/output

Abstract

The sea surface salinity (SSS) maximum of the South Indian Ocean (the SISSS-max) is a high-salinity feature centered at 30°S, 90°E, near the center of the South Indian subtropical gyre. It is located poleward of a region of strong evaporation and weak precipitation. Using several different satellite and in situ datasets, we track changes in this feature since the early 2000's. The centroid of the SISSS-max moves seasonally north and south, furthest north in late winter and farthest south in late summer. Interannually, the SISSS-max has moved on a northeast-southwest path about 1500 km in length. The size and maximum SSS of the feature vary in tandem with this motion. It gets larger (smaller) and saltier (fresher) as it moves to the northeast (southwest) closer to (further from) the area of strongest surface freshwater flux. The area of the SISSS-max almost doubles from its smallest to largest extent. It was maximum in area in 2006, decreased steadily until it reached a minimum in 2013, and then increased again. The seasonal variability of the SISSS-max is controlled by the changes that occur on its poleward, or southern, side, whereas intereannual variability is controlled by changes on its equatorward side. The variations in the SISSS-max are a complex dance between changes in evaporation, precipitation, wind forcing, gyre-scale ocean circulation and downward Ekman pumping. Its motion correlated with SSS changes throughout the South Indian Ocean and is a sensitive indicator of changes in the basin's subtropical circulation.

Plain Language Summary

The ocean surface is saltiest in the mid-latitude subtropics where evaporation is strong and precipitation is weak. Each ocean basin has such a region, centered 20-30° from the equator. These regions are sensitive indicators of a balance between the effects of the wind, evaporation, precipitation, and ocean currents. In this study, we focus on this salty region of the South Indian Ocean. It is centered around 30°S, 90°E, west of the coast of Australia. We have found variations in the size, saltiness and position of the feature. It shifts over a northeast-southwest path on a year-to-year basis and gets saltier and fresher at the same time. Our conclusion, is that this is largely a result of changes in the wind field and the shape and strength of the underlying ocean subtropical gyre. The motion we see is synchronized with similar motion of the analogous feature in the South Pacific, bringing up the likelihood of more global processes controlling both features.

1 Introduction

In five of the world's major ocean basins there is an area of the subtropical ocean characterized by a horizontal maximum of sea surface salinity (SSS), situated typically around 25° latitude (Gordon et al., 2015). The classical view of these features (Worthington, 1976; Gordon and Giulivi, 2014; Bingham et al., 2014; Katsura et al., 2013; Zhang and Qu, 2014; Bingham et al., 2019) has them being produced as a result of poleward Ekman transport underneath areas where evaporation greatly exceeds precipitation. At the latitude of the SSS maximum (the "SSS-max"), there is Ekman convergence and subduction as very salty water is incorporated into the interior circulation of the equatorward part of the subtropical gyre (Schmitt and Blair, 2015). These areas play a prominent role in the shallow overturning circulation (McCreary and Lu, 1994; Gu and Philander, 1997; Nonaka and Sasaki, 2007; Kolodziejczyk and Gaillard, 2012) which carries that salty water towards the equator, where it upwells and returns at the surface. SSS-max areas are closely associated with a strong excess of evaporation over precipitation (E-P), generally the strongest values in the global ocean (Schanze et al., 2010).

Thus, variability in the SSS maxima may be an indicator of changes in the global water cycle, or the magnitude of transfer of water from ocean to atmosphere. It may also indicate variability in internal ocean processes that are less well understood.

These SSS-max areas have been studied extensively in the northern hemisphere, especially in the North Atlantic (Lindstrom et al., 2015 and references therein), but have been less well characterized in the southern hemsiphere. The advent of satellite measurement of SSS (Lagerloef et al., 2008; Berger et al., 2002; Vinogradova et al., 2019), we can begin to understand how these areas move and change. There are suggestions that SSS in these areas may be increasing globally (Durack and Wijffels, 2010; Terray et al., 2012; Yu et al., 2020; Hosoda et al., 2009; Boyer et al., 2005) as the hydrologic cycle accelerates on a warming planet.

In the effort to understand the dynamics and variability of these features, we focus here on the SSS-max in the South Indian Ocean (the "SISSS-max") and its location within the greater South Indian Ocean (SIO) and atmospheric circulation. The SISSS-max is a much more elongated feature than the other ocean basins. The center is the farthest poleward of all the ocean basins (Gordon et al., 2015) at approximately (30°S, 90°E). Gordon et al. surmised that this is due to the Australia-Asian monsoon that pushes the intertropical convergence zone into the southern hemisphere, and to the injection of fresh water into the eastern Indian Ocean from the Bay of Bengal and through the Maritime Continent. The SSS of the feature does not vary much over the breadth of the SIO (Figure 1).

The main previous study of the SISSS-max is that of Wang et al. (2020 – henceforth "W20"). That study divided the SISSS-max into three separate features, one in the east just off of Australia, one in the center of the basin and a third in the western part of the basin near Africa. In the average picture of Figure 1, we do not detect an isolated SSS-max close to Australia and do not look as far west as the coast of Africa, but we focus on what W20 call the central maximum. It stretches from about 70°E to 110 °E and has SSS which reaches about 35.9 on average. The central maximum region identified by W20 starts at 90°E and stretches westward to 60°E, encompassing about half of the region identified in Figure 1. Our SISSS-max is a sort of combination of the eastern and central features of W20 as it encompasses the area shown in Figure 1.

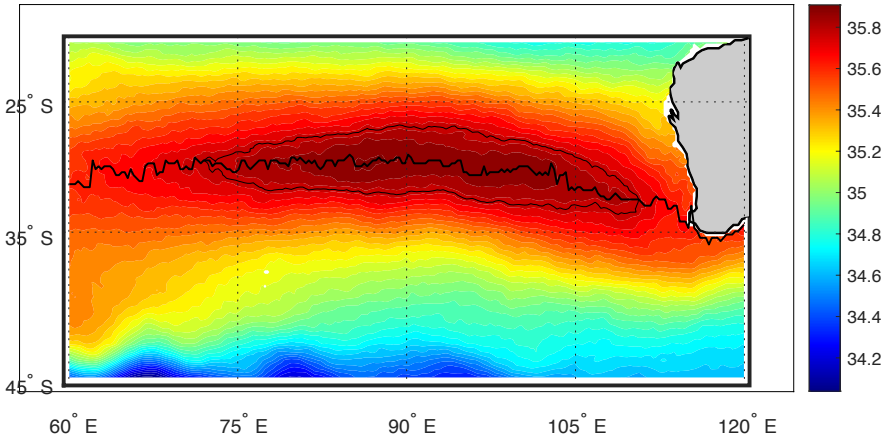

Figure 1. Mean SSS for the 2010-2020 period in the SIO from SMOS LOCEAN data. Color scale is at right. The thin black contour line marks SSS of 35.772 (a value used by Gordon et al.,

2015). The wiggly black line going from west to east is the latitude of maximum SSS at each longitude.

The SISSS-max is embedded in the SIO surface circulation, which a number of studies have described. As a typical example, Reid (2003) plotted the mean geostrophic flow. At 30°S, where the SISSS-max is located, the geostrophic part of the flow is very weak. The paper plots a meandering "S-shaped" flow more or less to the north through the SISSS-max. However, Reid notes that the surface circulation of the SIO is highly variable and that the type of averaging done was not ideal. Many studies of the SIO focus primarily on the tropical circulation, and have little to say about the flow in and around the SSS-max (e.g. Molinari et al., 1990; Han & McCreary, 2001; Menezes et al., 2013; Momin et al., 2015). Other studies of the subtropical SIO at the latitude of the SISSS-max come to much the same conclusion as Reid (2003), indicating weak flows at the surface, vaguely in the northward direction (W20; Stramma & Lutjeharms, 1997; Siedler et al., 2006; Schott et al., 2009; Palastanga et al., 2007; Menezes et al., 2014; Schott et al., 2002; Divakaran & Brassington, 2011). Maes et al. (2018), using an eddy-resolving model, identify an area of surface convergence in the SIO cenered at (30°S, 94°E). They also describe how the water from the region of the SISSS-max spreads from the South Indian into the South Pacific, perhaps leading to the formation of the secondary SSS-max in the western part of that basin (Gordon et al., 2015).

Below the surface, however, flows are better defined and more like what one might expect. At 200 db, Reid's (2003) mean flow turns by 90° relative to the surface and moves toward the northwest in a manner similar to what we might expect of a south equatorial current as the return limb of a subtropical gyre. This is similar to what we find in other ocean basins (e.g. Dohan et al., 2015; Bingham et al., 2019), and agrees with the sense of the wind-driven Sverdrup transport (Schott et al., 2002; Menezes et al., 2014). This northwestward-flowing interior circulation, however, does not seem to be associated with northwestward transport of salt. There is little sign of a distinct equatorward-westward spreading subsurface salt tongue (Han & McCreary, 2001) as is found in the North Atlantic (Schmitt & Blair, 2015), North Pacific (Katsura et al., 2013) or South Pacific (Kessler, 1999). Instead, the interior salinity distribution of the SIO is dominated by the low-latitude input of fresh water from the Pacific, via the straits and passages of Indonesia (Han & McCreary, 2001).

In contrast to the lack of well-defined surface circulation within the SISSS-max, areas to the north and south have distinct flow features. To the south, the Antarctic Circumpolar Current flows strongly to the east and also slants southward. This is visible in Figure 1 as a strong SSS front at 40-45°S (e.g. W20; Stramma & Lutjeharms, 1997). To the north, a current known as the South Indian Countercurrent (SICC) flows to the east in a highly variable banded pattern, with the southernmost band at around 25°S (Menezes et al., 2014; Menezes et al., 2016; Siedler et al., 2006; Palastanga et al., 2007; W20). In a contrasting view, Peng et al. (2015), using surface drifter data, do not show much of a SICC, except possibly in December and January. The area in the vicinity of the SISSS-max has relatively weak surface currents and mean and eddy kinetic energy. It is one of strong convergence as indicated by the way that drifters congregate at the very center of the SISSS-max (see their Figure 3).

The SISSS-max is the location of a minimum in mean wind stress (W20 – their Figure 2c). It is tucked between southeasterly trade winds, which reach down to around 25°S, and westerlies which come as far north as 35°S. It has positive wind stress curl throughout, indicating a prevalence of downward Ekman pumping (Qu et al., 2019). The wind stress pattern is

144 relatively steady throughout the seasons in a climatological sense (Schott et al., 2002). As a
145 result of this minimum of wind stress, the surface circulation appears to converge directly at the
146 latitude of the SISSS-max (Schott et al., 2002; Peng et al., 2015). This is in contrast to the all
147 other ocean basins with SSS-maxima, where Ekman transport is poleward through the SSS-max
148 (Gordon et al., 2015). The SIO has a larger eddy kinetic energy than the other southern
149 hemisphere ocean basins, and as a result has a large eddy flux of salt, and the SISSS-max is also
150 a maximum of convergence of salt flux (Qu et al., 2019). Thus, horizontal eddy flux of salt plays
151 a larger role in the SIO than in other ocean basins.

152 W20 give a basic description of the SISSS-max. It is situated well to the south of the
153 maximum of surface freshwater forcing which is around 10-20°S. SSS within their central
154 maximum has a seasonal cycle, with highest value in April, i.e. fall. They computed budgets for
155 the eastern, central and western SSS-maxima, both seasonally and interannually (2011-2015).
156 For the central maximum, defined as a box with limits (35-28°S, 60-100°E), the budget was not
157 closed in either case. The SSS tendency fluctuated strongly, but was not matched by a surface
158 forcing, advection or vertical entrainment term. The tendency computed from satellite (Aquarius)
159 data is very different from that computed from Argo data. The magnitude of tendency variability
160 - it fluctuates on a scale of approximately +- 0.04 month^{-1} – is similar to other ocean basins (e.g.
161 Dong et al., 2015; Katsura et al., 2013).

162 In this paper, we expand on the work of W20, to better define the seasonal cycle, and
163 look at longer-term trends in the location and scope of the central SISSS-max. We relate the
164 SISSS-max to the surface forcing and underlying subtropical gyre, in light of the results
165 summarized above.

166 **2 Data and Methods**

167 Gordon et al. (2015) delineated the SISSS-max using the 35.772 isohaline at the surface,
168 a convention we adopt here (Figure 1). This threshold isohaline value is derived from the
169 MIMOC (Monthly Isopycnal/Mixed layer Ocean Climatology; Schmidtko et al. (2013)). We
170 compute the area with this value of SSS or higher and the location of the centroid of this area in
171 order to quantify the variability. We also compute and display values of surface flux in the
172 region as well as the advection and entrainment terms in the salinity balance equation.

173 2.1 Data

174 See Acknowledgements section for details on version number and data access for all
175 datasets used.

176 There are several SSS datasets displayed, Two SMOS, two SMAP, one Aquarius, one L4
177 composite and two in situ gridded (Table 1). All SSS datasets where retrieved from the source
178 either as monthly averages, or averaged monthly after retrieval. The in situ data used are the EN4
179 dataet of Good et al. (2013), and the Roemmich and Gilson (2009) dataset (the "RG" data).

180

Dataset name	Spatial grid size	Dates	Color in Figures 2-5
SMOS LOCEAN	0.25°	2010-December 2020	Yellow and black
SMOS BEC	0.25°	2010- December 2020	Red

SMAP JPL	0.25°	2015- December 2020	Green
SMAP RSS	0.25°	2015- December 2020	Black dashed
Aquarius	1°	2011-2015	Green
CCI - composite	0.25°	2010-2018	Black solid
EN4 – in situ	1°	2004*- December 2020	Blue
RG – in situ	1°	2004*-December 2020	Cyan

*EN4 and RG data go further back, but we chose to start at 2004.

Table 1. Names, spatial grid size and dates for SSS datasets used.

A few other datasets are used. The EN4 data, mentioned above, has a subsurface component, from which we compute dynamic height relative to 2000 m depth.

We used the OSCAR surface current dataset (Bonjean & Lagerloef, 2002) to determine surface flows.

Wind data are from the NCEP/NCAR reanalysis (Kalnay et al., 1996).

Freshwater forcing is defined as

$$FWF = S_0 \frac{E - P}{h}$$

where S_0 is a constant, set to 35, E is evaporation, P precipitation and h the mixed-layer depth. Evaporation data are monthly averages sourced from the OAflux dataset of Yu & Weller (2007). Precipitation are monthly values from IMERG (Integrated Multi-satellitE Retrievals for GPM; Skofronick-Jackson et al., 2018). Evaporation and precipitation data are interpolated onto a 1°X1° grid. We used a monthly climatological 1° mixed-layer depth product from MIMOC (Monthly, Isopycnal/Mixed-layer Ocean Climatology; Schmidtko et al., 2013). This product computes the mixed-layer depth following the method of Holte & Talley (2009). We tried some other non-climatological mixed-layer products and found them to be not useful for our purposes.

Vertical velocity values are computed from upwelling and the vertical motion of the bottom of the mixed layer. Upwelling data were downloaded from NOAA Coastwatch. Entrainment was computed by combining vertical velocity with the vertical salinity gradient following the method of Bingham et al. (2010).

2.2 Methods

The area of the SISSS-max is defined here as the area with SSS higher than the threshold in the central SIO (60-120°E, 20-45°S). The meridional (zonal) centroid is the latitude that half of the area is to the north (east) of in the central SIO. The meridional northern (southern) limit is the latitude that 95% of the area with SSS higher than the threshold is south (north) of. Similar definitions apply for the east/west limits of the feature. This calculation was done monthly.

We note here that there is a close relationship between average SSS (or maximum SSS) within the threshold isohaline and area. That is, when the area within the threshold isohaline is

large the water within it is also salty as can be seen in Figure 2. This close relationship holds better for small values of area and gets more scattered as the area gets larger. What Figure 2 shows is that the isohaline area in the SIO is mainly a measure of how salty the water within the SSS-max is, both on a monthly and a yearly basis. On both monthly and yearly time scales the two are significantly correlated. This conclusion may seem self-evident, but it is worth confirming nonetheless.

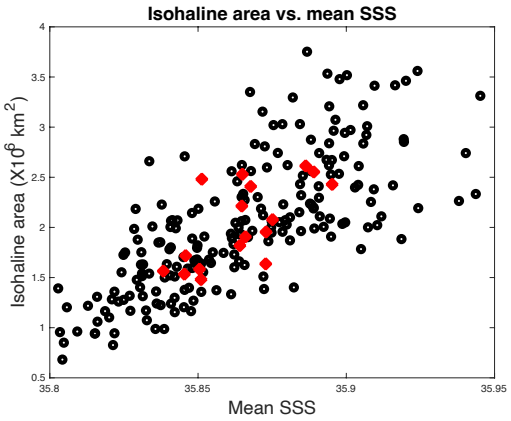

Figure 2. Mean SSS computed within the 35.772 isohaline vs. area with SSS>35.772 from EN4. Black symbols are monthly (areas are the same data displayed in Figure 6). Red symbols are yearly averages (areas are the same data displayed in Figure 8).

3 Results

The area of SSS greater than 35.772 (Figure 3) shows a range of values and changes among the different products. For the SMAP JPL product, the area appears to nearly quadruple between 2015 and 2020 from 0.5 to 2.0X10^6 km^2. The BEC product shows an increase, but not to the same degree, from about 1.5 to 2.5X10^6 km^2. The EN4 and SIO data have a maximum in 2017-2018, but generally increase from 2010 to 2020. The LOCEAN product has more variation than any of the others, and tends to have larger values, but with a strong decrease from 2012 to 2020. The Aquarius, CCI and RSS SMAP products do not show much change over the time period they are depicted in Figure 1. There is seasonal variability in the different products too, with maximum SSS in summer (January-March) and minimum in winter (July-August) (Gordon et al., 2015). This seasonality is more difficult to detect in the CCI, LOCEAN and BEC products, but quite apparent in the EN4, SIO, Aquarius and the two SMAP products.

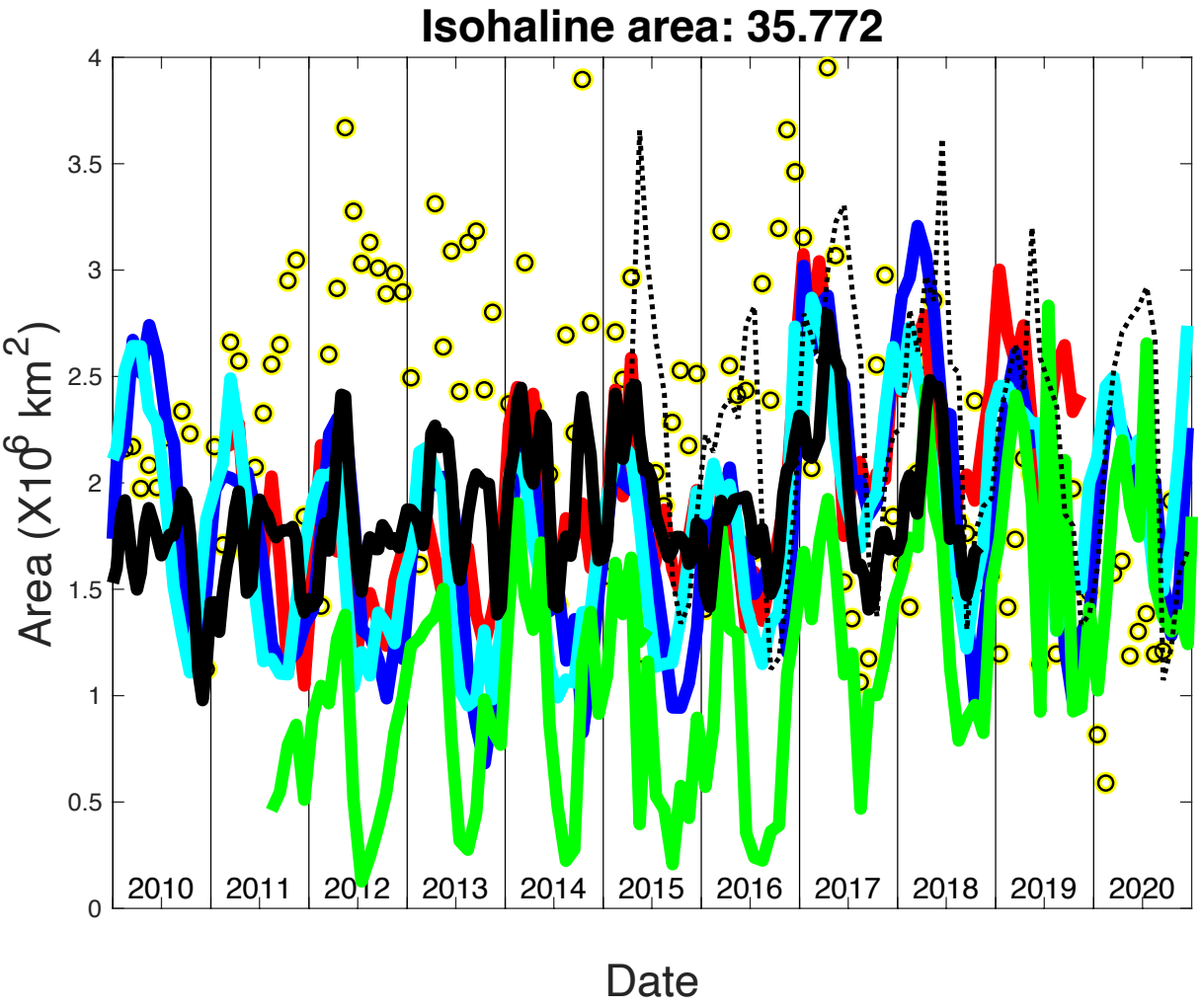

Figure 3. Area with SSS greater than 35.772 as a function of time with units of 10^6 km^2. The different colors represent different satellite and other products, with a color key in Figure 4. Note, the JPL SMAP and Aquarius products are the same color (green) and overlap by a couple of months in early 2015.

The different datasets are much more consistent when it comes to showing the changing position of the feature. In the north-south direction (Figure 4) the datasets have consistent intetrannual and seasonal changes. The SISSS-max moved steadily equatorward between 2010-2011 and 2020, with total motion of 0.5-1°. This is apparent in every dataset, but to different degrees. The EN4 dataset starts out with the centroid at 30.5-31°S in 2010-2011, and it moves northward to 29.5°S in 2020, with a large excursion southward in 2015. There is significant seasonality as well in this north-south motion. The feature is furthest south in summer and north in winter, as seen consistently in all the datasets. The amplitude of the seasonal north-south motion is 1-1.5°.

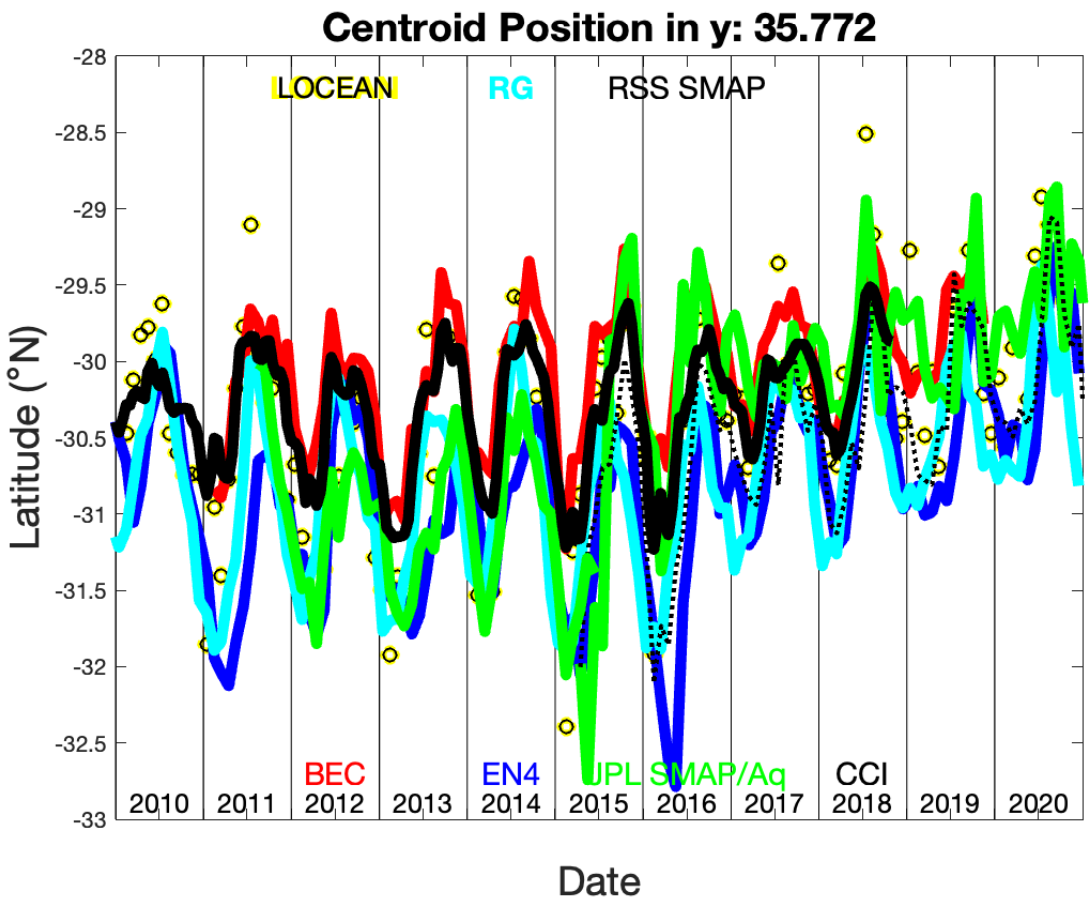

Figure 4. Latitude position of the centroid of the 35.772 isohaline in the SIO. The different dataset are keyed to colors as shown at the bottom of the figure. The RSS-SMAP curve is dashed. Note, the JPL SMAP and Aquarius products are the same color (green) and overlap by a couple of months in 2015.

The longitude position of the centroid (Figure 5) is more variable within products, but again the different products are relatively consistent with each other. Between about 2011 and 2020, the position of the centroid moves significantly eastward, from about 87°E to about 99°E, a distance of over 1000 km. There are large excursions during this time. In 2016, the feature moves far eastward, past 100°E. In 2013, the feature moved far waestward, to 80-85°E. This westward motion is also detected in 2012, 2014 and 2018, but only by the JPL SMAP and Aquarius products. Seasonal variability in the longitude position of the SISSS-max is not apparent in this display.

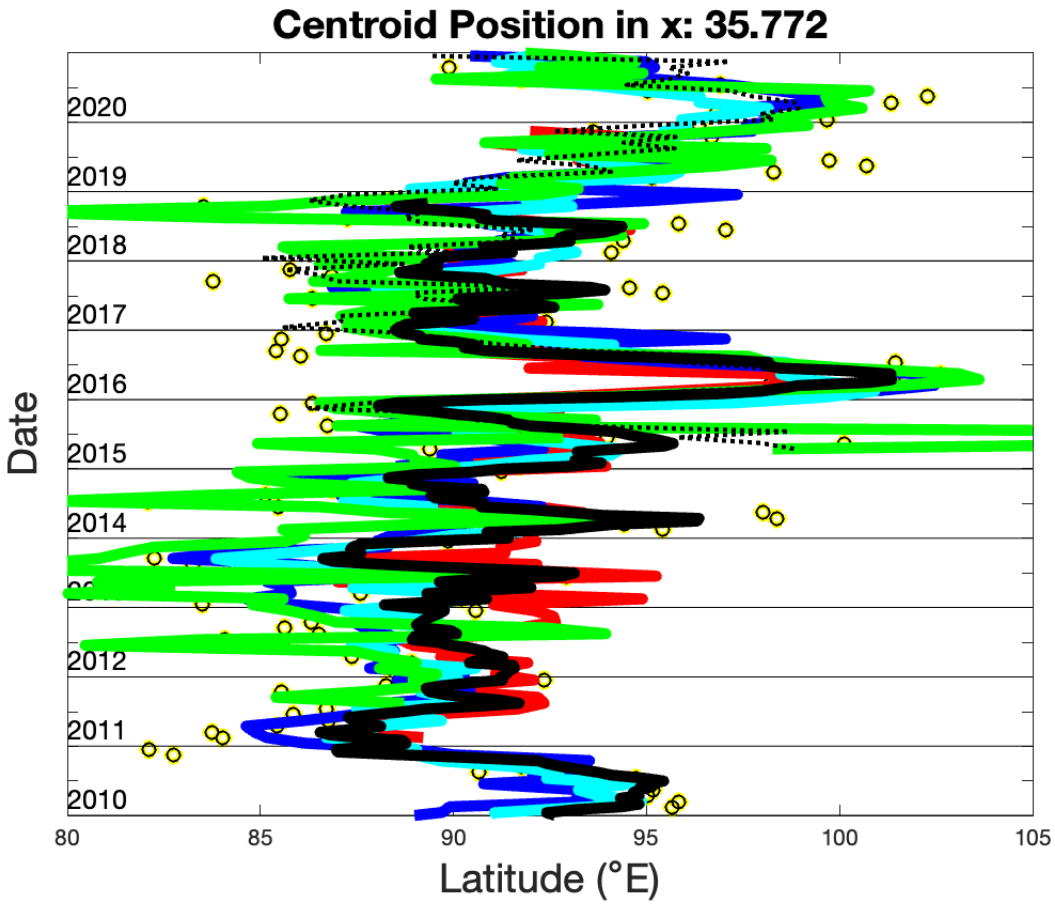

Figure 5. Longitude position of the centroid of the 35.772 isohaline in the SIO. The different dataset are keyed to colors as shown in Figure 3. The RSS-SMAP curve is dashed. Note, the JPL SMAP and Aquarius products are the same color (green) and overlap by a couple of months in 2015.

The in situ data give an idea of the trends in position and area over a longer time scale (Figure 6), and a number of items can be noticed. The seasonal cycle in area changes in amplitude. From 2004-2008, the range of the seasonal cycle is about 2 X10^6 km^2. After that, there appears to be some kind of regime shift, where the range decreases to about 1 X10^6 km^2 and the area decreases, until about 2013. After that, the area increases again, and the range does as well. The latitude shifts in tandem with the area. It starts out at close to 30°S. It then shifts southward for several years until about 2013, when it reaches a southward excursion of about 31.5°S. After that it again moves northward.The latitude has a seasonal cycle with a range of 1-1.5°, but it remains about the same amplitude throughout. The longitude position (lower panel) does not have a visible seasonal cycle, but does have interannual variability in sync with the area and latitude. The feature moves farthest west in 2013 to about 85°E. Before and after that it is further east as far as 100°E in 2016.

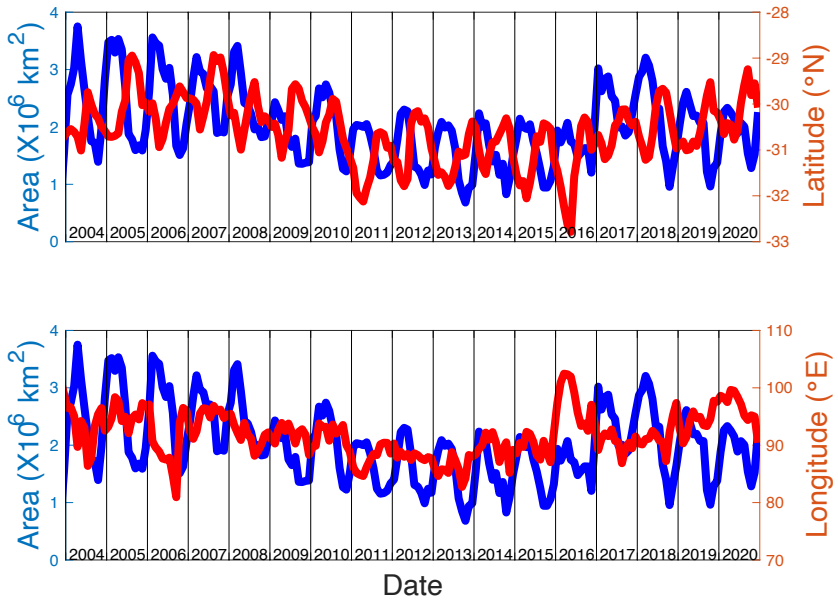

Figure 6. From EN4 data. Top panel: Blue curve/left axis, area with SSS>35.772. Red curve/right axis, latitude position of the centroid. Lower panel: Blue curve/left axis, area with SSS>35.772, same as top panel. Red curve/right axis, longitude position of the centroid. Blue curves are the same in each panel.

Putting the east-west and north-south motion together into an annual average (Figure 7), we see that the SISSS-max shifts substantially along an almost linear southwest-northeast path. The southwestern limit was reached in about 2013 (green contour) and the northeast limit in 2020 (black and yellow contour). 2016 was a bit of an exception: The SISSS-max was farther east, but shifted to the south as well. This is due to one event that occurred in March-April of that year as can be seen in Figure 6. The size is also correlated with these motions. As the feature moves to the northeast it gets larger and smaller when it moves to the southwest.

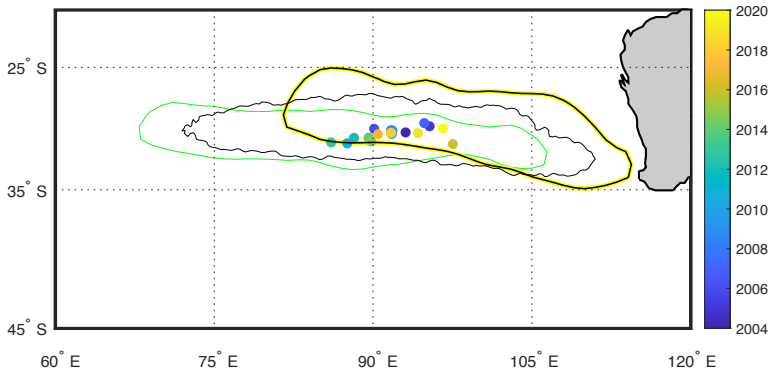

Figure 7. Annual-average centroid position. The symbols are color-coded by year with the scale at right. The light black line is the annual average 35.772 contour from Figure 1. The green line is the same contour averaged for 2013, when the area is minimum and the feature is far to the southwest. The yellow and black line is for the year 2020, when the area is large and the feature is far to the northeast.

The yearly average area (Figure 8) shows large changes in area over time. The area ranges from a high of 2.6 $X10^6$ km^2 in 2006 down to a low of just over 1.4 $X10^6$ km^2 in 2013, a decrease by a factor of almost ½ in 7 years. The area abruptly increased again to another maximum in 2017 and another sharp decrease. The overall picture is of a feature with large coherent interannual changes. Putting this change in area together with the motion in Figures 4-7, the SISSS-max gets smaller as it moves to the southwest and larger as it moves northeast.

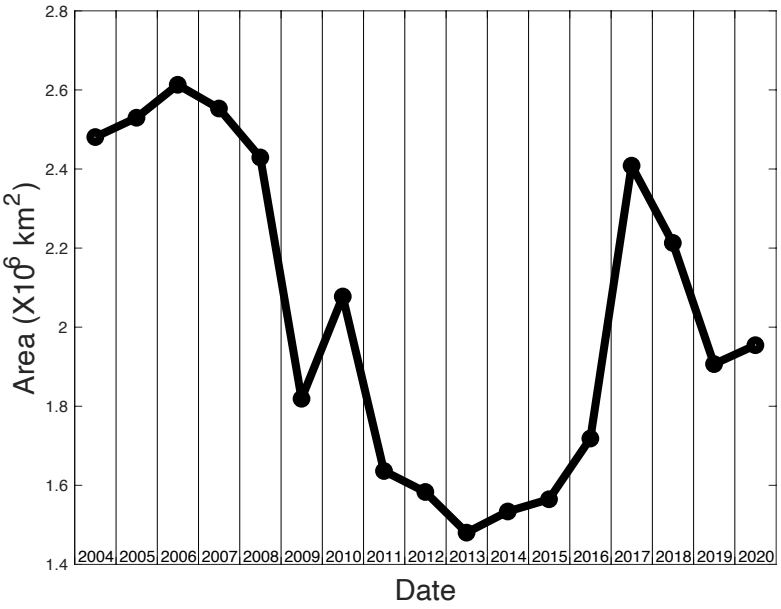

Figure 8. Annual average area of SSS>35.772 in the SIO from EN4 data.

We can learn more about what causes the observed variability of the SISSS-max by looking at the limits of the feature (Figure 9). As noted before, the SISSS-max moves north and south over the course of the year. It is clear from Figure 9a that most of that change is a result of the motion of the poleward boundary, which has a large seasonal cycle of range about 3°. This seasonal motion occurs every year, though the size of it changes, being larger in some years (e.g. 2016) and smaller in others (e.g. 2004). By contrast, the interannual variability of the SISSS-max position is mainly determined by the equatorward boundary. This has no discernable seasonal cycle, but large interannual changes. It moves from close to 25°S in 2005, down to about 29°S in 2013. It is hard to detect any seasonal cycle in the east-west motion of the SISSS-max (Figure 9b). It has interannual variability as discussed above, but that is not dominated by either the eastern or western side. It does look like the western side of the feature is more highly variable in position then the eastern side.

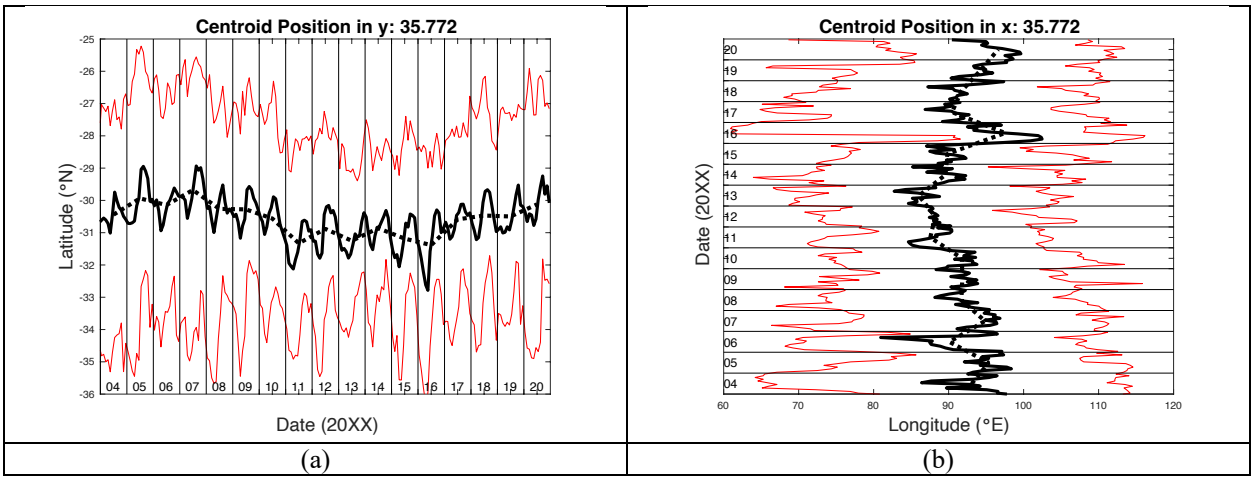

Figure 9. From EN4 data. a) Black curves: Latitude of the centroid of the SISSS-max. Solid curve is monthly, dashed curve is the yearly average. This is the same as the red curve in Figure 5 upper panel. Upper (lower) red curve: latitude of the 95th percentile of area. That is, 95% of the area with SSS>35.772 is south (north) of this latitude. b) As in panel a) but for the longitude of the centroid and with time on the y-axis.

One can see how the SISSS-max fits into the larger scale variability of the SIO on an interannual time scale by looking at the correlation between the area (Figure 8) and the SSS over the larger SIO (Figure 10). The pattern is quite striking. North of the SISSS-max, the correlation is positive, with values as high as 0.8. South of the SISSS-max, the pattern is opposite, negative correlations with some very low values. The boundary, with near-zero correlation, runs along the northern edge of the SISSS-max. This explains the northeast-southwest translation shown in Figure 7. As the SISSS-max moves to the northeast, the area gets larger and SSS within the feature increases. As it moves to the southwest, the area gets smaller and the SSS decreases. The highest positive correlations are near the west coast of Australia. The SISSS-max moves closer to there as it gets saltier and larger as seen in Figure 7. This picture puts the SISSS-max within a large scale see-saw pattern in the SIO, high SSS in the lower latitudes corresponding with low SSS in higher latitiudes, and vice versa. It should be noted that the picture in Figure 10 is based on only 17 years of data, so does not have a high degree of statistical confidence.

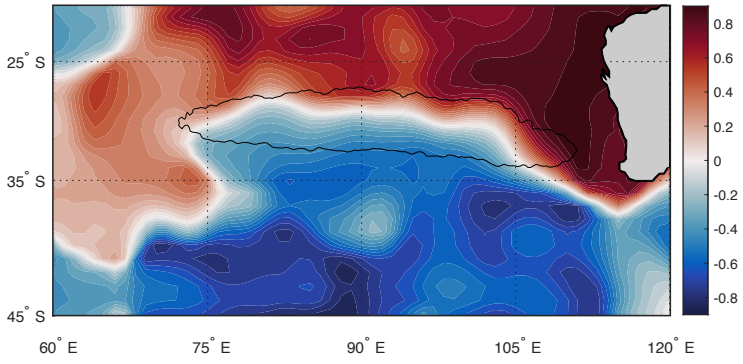

Figure 10. Unitless correlation between annual average area (Figure 8) and annual-average SSS at each location in the SIO. Data are from the EN4 dataset over the 2004-2020 time period. Thin black line is the mean 35.772 isohaline as in Figure 1.

As discussed above, the SISSS-max is embedded in the SIO circulation, and is impacted by winds and freshwater forcing the surface. In the (2010-2020) mean, the SISSS-max sits within a region that is evaporation-dominated (red area in Figure 11). The boundary between evaporation and precipitation-dominated regions crosses the study area diagonally from (27°S, 60°E) to (42°S, 120°E). The SISSS-max is to the northeast of this delineation, similar to the South Pacific (Bingham et al., 2019). The feature is located to the southwest of where the freshwater forcing is most strongly positive, which in Figure 11 is 20-25°S (see also Gordon et al., 2015, Figure 1b). This placement is similar to that of the SSS-max in the Soutth Pacific (Bingham et al., 2019). Again as discussed in the introduction, the underlying geostrophic circulation is very weak, especially poleward of the SISSS-max. It is more or less northward from the Antarctic Circumpolar Current (ACC) at 40-45°S to the SISSS-max. At a latitude of about 30°S, in the middle of the SISSS-max, the flow strengthens and takes a right-hand turn towards the Australian continent.

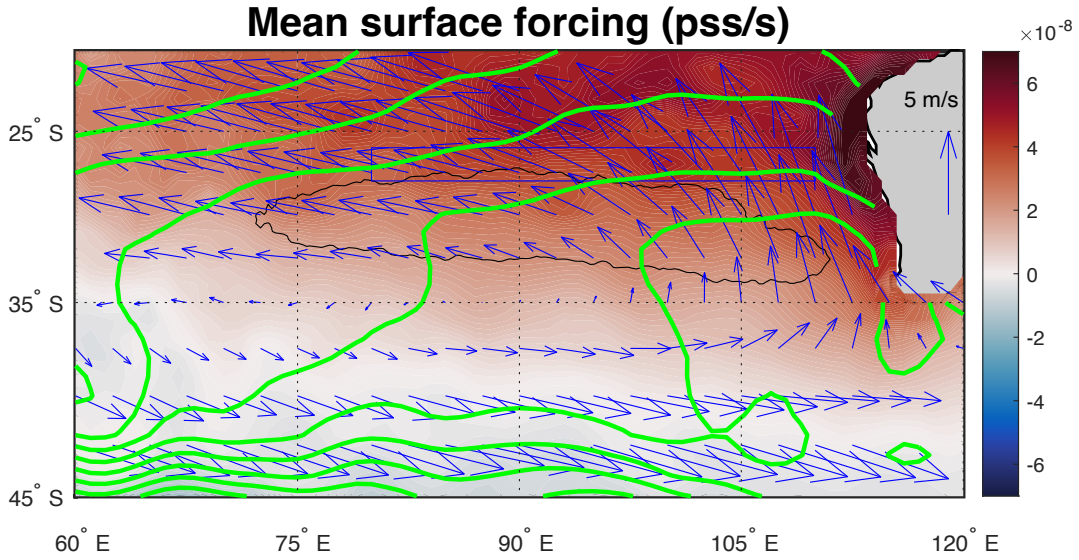

Figure 11. Averages over 2004-2019. Colors: freshwater forcing (see equation 1). Color scale is at right, with units of pss/s. Positive (red) values indicate freshwater forcing out of the ocean, i.e. net evaporation. Green contour lines: dynamic height at the surface relative to 2000 m from EN4 data, with units of dynamic-meters and a contour interval of 0.1. Arrows: mean winds from NCEP. A 5 m s^{-1} scale arrow is displayed at right on top of the Australian continent. Light black line is the SSS=35.772 contour as in Figure 1. Small box (80-110°E, 26-28°S) is where the average in Figure 13 is taken from.

The wind field that impacts the SISSS-max varies with time. The most relevant variation occurs near the coast of Australia at (30°S, 110°E), with minimum seasonal speed in winter (Figure 12). The seasonal aspect of this variability has the SIO subtropical high depicted in Figure 11 getting stronger and weaker at this location, or, alternatively, moving equatorward and poleward. The high is furthest equatorward in winter, and thus winds are weak. This north-south

shifting of the winds may relate to the seasonal changes in the SISSS-max at its poleward edge. Perhaps when the winds are strongest there in summer, evaporation increases and so does the SSS. The interannual variability at this location indicates weak winds in the 2011-2014 time period, coincident with the minimum in area shown in Figure 8.

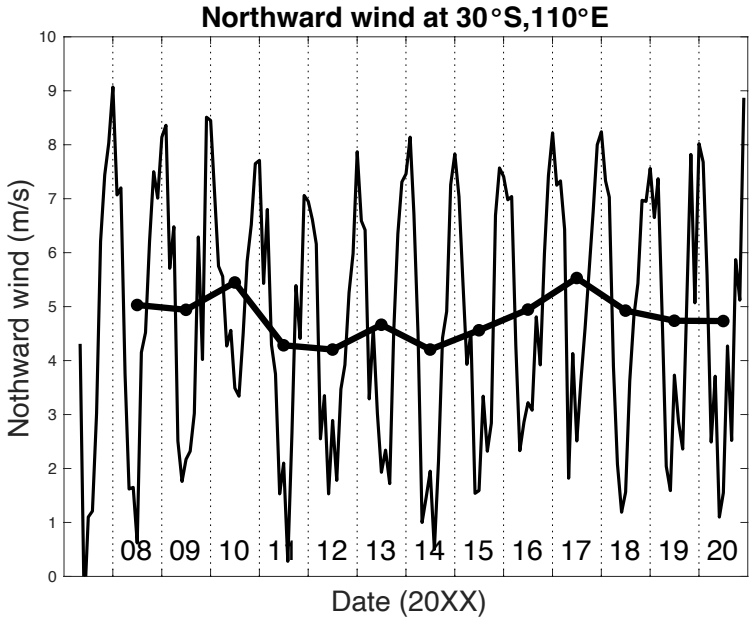

Figure 12. Northward wind at (30°S, 110°E). Variable black line is from monthly averages. Smoother black line with symbols is a yearly average.

Given that the SISSS-max is closely linked to the surface forcing, it would be logical to conclude that variability of the forcing in the area equatorward of the feature is related to the area or motion. However, this does not seem to be the case. E-P averaged within the box in Figure 11 is quite variable on short time scales, but relatively steady interannually (Figure 13). There is a small dip in 2018 due to three anomalous months at the end of the year. Given this result, it seems variability of E-P just equatorward of the SISSS-max does not directly control SSS variability or the size or position of the feature.

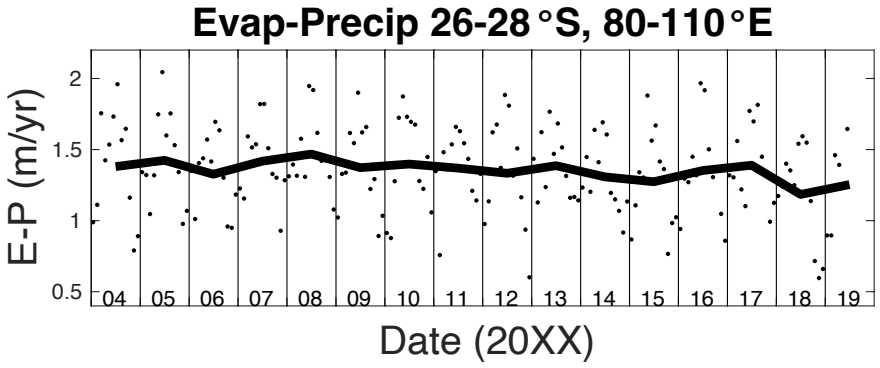

Figure 13. E-P (m/yr) averaged over the box shown in Figure 11. Black dots are monthly values. Black curve is yearly averages.

As shown in Figure 11, the gyre-scale geostrophic flow beneath the SISSS-max is northeastward, more or less opposite to the Ekman component. The geostrophic flow across 27°S is indicated by the dynamic height between 80 and 110°E. The sea surface slopes generally downward from west to east, consistent with net northward motion. There is an O(20 cm) height difference from west to east (Figure 14). The gradient across the breadth of the SISSS-max varies from year-to-year, but comes to a minimum in the years 2011-2015. These are the same years in which the area of the feature reached a minimum and it translated farthest to the southwest. Thus, the large-scale gyre flow appears to have some control over (or is at least correlated with) the position and size of the SISSS-max.

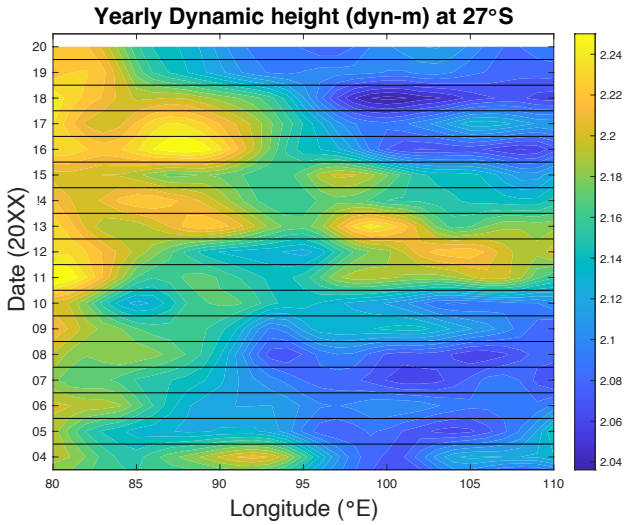

Figure 14. Yearly-averaged dynamic height (in dyn-m) from EN4 data along 27°S as a function of time.

We have computed the advection term in the salinity balance equation (Figure 15). The mean values are small (not shown), but the variability has an interesting distribution. The advection term is quite variable on the equatorward side of the SISSS-max, but there is much less variability within the feature and on the poleward side. This emphasizes the importance of eddy processes in bringing fresh water to the SISSS-max (Johnson et al., 2016) from the tropics and the salinification that accompanies that transport. On the other hand, eddy advection plays a much smaller role on the poleward side of the SISSS-max.

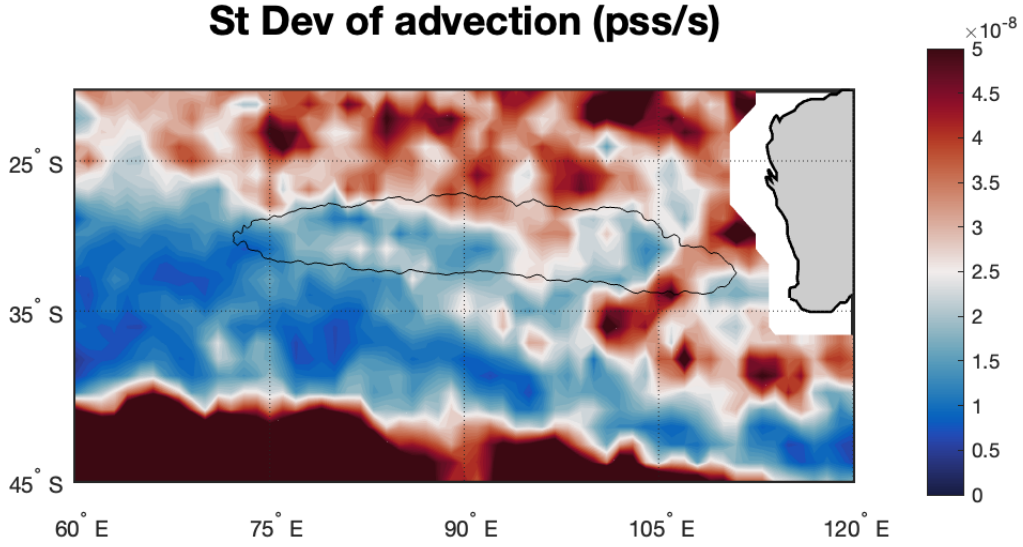

Figure 15. Standard deviation of the advection terms of the salinity balance equation. Light black line is the SSS=35.772 contour as in Figure 1.

The entrainment term of the salinity balance equation is more easily interpreted than the advection. The term itself is very small in the mean compared to other terms (not shown), but the distribution of variability relative to the SISSS-max is interesting (Figure 16). There is a local maximum in the amount of variability of the entrainment term at the poleward edge of the SISSS-max. Examination of individual records (not shown) indicates that the poleward-edge variability is mainly seasonal, with upwelling peaking in winter. This is likely the source of the seasonal changes observed at the poleward edge of the SISSS-max (Figure 9b). During the winter upwelling mixes fresh water into the surface and decreases the observed size of the SISSS-max, where as in summer, that process reverses and exchange with the interior goes in the opposite direction, having little impact on the surface salinity balance. Variability of entrainment at the equatorward edge of the SISSS-max is much smaller. Additionally, because of the vertical distribution of salinity, vertical entrainment at the equatorward edge of the SSS-max would add salty water to the surface mixed layer, not fresh. Strong seasonal vertical entrainment at the poleward edges of all the major SSS-max features has been noted before (Johnson et al., 2016).

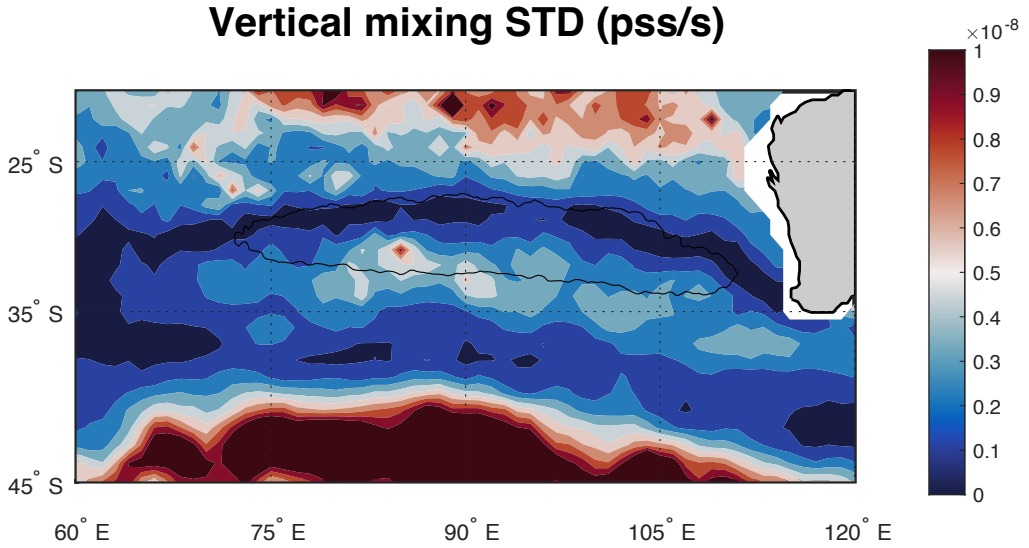

Figure 16. Standard deviation of the vertical mixing term (pss/s) in the SIO. Light black line is the SSS=35.772 contour as in Figure 1.

4 Discussion

The SIO SSS-max has been shown to vary on seasonal and interannual time scales in its position (Figures 4-7), size (Figures 3 and 6-8) and intensity (Figure 2). Its centroid moves in a distinct northeast-southwest track (Figures 6 and 7) for reasons that are still not entirely clear, but may relate to the balance between Ekman transport and the geostrophic flow of the subtropical gyre. The flow of the subtropical gyre tends to push the feature to the northeast, while Ekman transport pushes it to the southwest. The fact that the SISSS-max is situated to the northeast of the minimum of the mean winds (Figure 11) bears this out. The apparent correlation between position and size/intensity makes sense. As the feature moves northeastward, it moves into an area more dominated by evaporation (Figure 11) and thus gets saltier.

Advection is small within the SISSS-max relative to surrounding areas (not shown). This makes sense as the SSS gradient becomes small near the meridional peak of SSS - advection is the dot product of the velocity and SSS gradient. So a determining factor in the size, position and intensity of the SISSS-max may be not so much the strength of evaporation at the center of the feature, but the evaporation imposed on the source waters as they flow towards it, and the amount of time that water spends underneath this strong evaporation while in transit (D'Addezio & Bingham, 2014; Bingham et al., 2014).

We have not explicitly addressed the role of eddy advection of salt in the variability of the SISSS-max. Eddy processes may be more of a factor in the SIO than in other oceans due to elevated eddy kinetic energy in the SIO, especially on the equatorward side. Qu et al. (2019) emphasize this point showing a large divergence of the salt flux centered at the SISSS-max. Johnson et al. (2016) also describe the importance of eddy over mean advection. Though the eddy flux may be important in the mean location of the SISSS-max, it is not clear how or if eddy processes may contribute to the variability of the position or size. Are there interannual changes in the strength of eddy advection?

458 The main seasonal variation in the SISSS-max is expansion and contraction on the
459 poleward side (Figure 9a). We have discussed the likely role of seasonal variability in vertical
460 entrainment in this. Vertical entrainment shifts from downwelling to upwelling and back again
461 over the course of the year. Vertical processes are driven by the curl of the wind stress and the
462 heaving of the base of the mixed layer. The prevailing winds (Figure 11) indicate that the mean
463 zero in wind stress is found south of the SISSS-max, at about 35°S. Seasonal shifting in the
464 strength and distribution of the wind stress curl may be the cause of the observed seasonality in
465 vertical entrainment (Figure 16) and thus the poleward edge of the SISSS-max. Bingham et al.
466 (2021) have shown that there is a strong seasonal cycle in the small-scale (<100 km) variance of
467 SSS in the vicinity of the SISSS-max, with maximum in the fall season. This is likely due to
468 seasonal variation of rainfall. How this might impact the expansion and contraction of the
469 SISSS-max on its poleward side is still an open question.

470 The close relationship of the SISSS-max to the wind field is emphasized in Figures 11
471 and 12. Varibility of the wind field can impact the SISSS-max in several different ways, through
472 Ekman transport which advects water towards the feature, through Ekman convergence which
473 determines the structure of the underlying subtropical gyre and also causes SSS-max water to
474 subduct and enter the interior flow, and through changes in evaporation which is closely tied to
475 wind speed. Future research can help sort out which of these is most important in helping to
476 shape the structure of the SISSS-max.

477 The SISSS-max in the eastern Indian Ocean is also influenced by the input of low salinity
478 water from its equatorward side. The surface layer and thermocline off the northwest coast of
479 Australia has low salinity, mainly due to Indonesian Throughflow (ITF). This results in relatively
480 high sea level that induces a north to south pressure gradient off the west coast of Australia,
481 driving the southward flowing Leeuwin Current (LC) (Gruenberg, 2021). The poleward flowing
482 LC is an unusual subtropical gyre eastern boundary current, which in other oceans flows towards
483 the equator. The north-south pressure gradient is more effective in sending low salinity water
484 into the LC when the northward winds relax which truncates the eastern extension of the 35.772
485 isohaline.

486 Bingham et al. (2019) studied the SSS-max in the South Pacific in a similar way as we
487 have done here, and found similar variability in the centroid. There was a minimum in area, but
488 1-2 years before the one we have shown in this paper in the South Indian. The fact that the two
489 SSS-maxima behave in similar ways suggests that their motion is a result of similar forces, or
490 that one influences the other. In the South Pacific Bingham et al. suggested that the variability is
491 linked to the Pacific Decadal Oscillation (PDO), and found significant correlation between the
492 PDO index and the annul-average area. There was a minimum in PDO in 2009, and a minimum
493 in SSS-max area in 2011. Thus, the SSS-max area in the South Pacific lags the PDO by ~2 years,
494 and, by extension, the lag between PDO and SISSS-max area is ~3-4 years. Perhaps the
495 increased delay in the SIO results from the fact that the SISSS-max is 5° poleward of that of the
496 South Pacific. Another possibility is the role of the ITF in connecting the Pacific and Indian
497 ocean basins that adds a time delay in the Indian Ocean response relative to the Pacific.
498 Regardless of the reason, the syncronicity of the motion of the centroid in the South Pacific and
499 South Indian emphasizes the interconnectedness of the two ocean basins (Qu et al., 2019).

500 As stated above, the SISSS-max is the result of a delicate balance between a number of
501 competing and complementary processes, northeastward motion due to the underlying
502 subtropical geostrophic circulation, southwestward motion due to Ekman transport, vertical

entrainment variability at the poleward edge, eddy advection in the region equatorward of the SISSS-max and a predominance of evaporation over precipitation which decreases towards the southwest. All of these have a role in determing the position, size, intensity and variability of the feature. The SISSS-max can change in response to changes in any of these processes. Thus, the SISSS-max is a sensitive indicator of the climate of the SIO, and of the southern hemisphere subtropics in general. In order to understand the balance of forces affecting the interannual variability of the SISSS-max, one has to study not just the processes within it, but the variability of the source waters, the wind systems that drive Ekman transport and downwelling and the eddy transport on the equatorward side.

Acknowledgments and Data

Funding was provided by NASA under grants 80NSSC18K1322 and 19-OSST19-0007.

Data used in this paper are obtainable from the following sources:

- NCEP/NCAR Reanalysis winds (Kalnay et al., 1996): https://psl.noaa.gov/data/gridded/data.ncep.reanalysis.derived.html
- SMOS LOCEAN V5: https://data.catds.fr/cecos-locean/Ocean_products/L3_DEBIAS_LOCEAN/L3_DEBIAS_LOCEAN_v5/debiasedSSS_09days_v5/
- SMOS BEC: http://bec.icm.csic.es/ocean-experimental-dataset-global/
- SMAP JPL: https://doi.org/10.5067/SMP50-3TMCS
- SMAP RSS: https://data.remss.com/smap/SSS/V05.0/FINAL/L3/monthly/
- Aquarius: https://doi.org/10.5067/AQR50-3YMCE
- CCI: https://doi.org/10.5285/9ef0ebf847564c2eabe62cac4899ec41
- EN4: https://www.metoffice.gov.uk/hadobs/en4/download-en4-2-2.html
- RG: http://sio-argo.ucsd.edu/RG_Climatology.html
- OAFlux: https://oaflux.whoi.edu/data-access/
- IMERG: https://gpm.nasa.gov/data/directory
- Ekman upwelling: https://coastwatch.pfeg.noaa.gov/erddap/griddap/erdQAstressmday.html

References

Berger, M., et al. (2002), Measuring Ocean Salinity with ESA's SMOS Mission, ESA Bulletin, 111, 113-121.

Bingham, F. M., J. Busecke, A. L. Gordon, C. F. Giulivi, and Z. Li (2014), The North Atlantic subtropical surface salinity maximum as observed by Aquarius, Journal of Geophysical Research: Oceans, 119(11), 7741-7755, doi:10.1002/2014JC009825.

Bingham, F. M., J. J. M. Busecke, and A. L. Gordon (2019), Variability of the South Pacific Subtropical Surface Salinity Maximum, Journal of Geophysical Research: Oceans, 124(8), 6050-6066, doi:10.1029/2018JC014598.

Bingham, F. M., G. R. Foltz, and M. J. McPhaden (2010), Seasonal cycles of surface layer salinity in the Pacific Ocean, Ocean Science, 6, 775-787, doi:10.5194/os-6-775-2010.

Boyer, T. P., S. Levitus, J. I. Antonov, R. A. Locarnini, and H. E. Garcia (2005), Linear trends in salinity for the World Ocean, 1955–1998, Geophysical Research Letters, 32(1), doi:10.1029/2004GL021791.

D'Addezio, J. M., and F. M. Bingham (2014), A subtropical North Atlantic regional atmospheric moisture budget, Journal of Geophysical Research C Oceans, 119(12), 8731-8748, doi:10.1002/2014JC010300.

Divakaran, P., and G. B. Brassington (2011), Arterial ocean circulation of the southeast Indian Ocean, Geophysical Research Letters, 38(1), doi:10.1029/2010GL045574.

Dohan, K., H.-Y. Kao, and G. S. E. Lagerloef (2015), The freshwater balance over the North Atlantic SPURS domain from Aquarius satellite salinity, OSCAR satellite surface currents, and some simplified approaches, Oceanography, 28(1), 86–95, doi:10.5670/oceanog.2015.07.

Dong, S., G. Goni, and R. Lumpkin (2015), Mixed-layer salinity budget in the SPURS region on seasonal to interannual time scales, Oceanography, 28(1), 78–85, doi:10.5670/oceanog.2015.05.

Durack, P. J., and S. Wijffels (2010), Fifty-Year Trends in Global Ocean Salinities and Their Relationship to Broad-Scale Warming, Journal of Climate, 23(16), 4342, doi:4310.1175/2010JCLI3377.4341.

Good, S. A., M. J. Martin, and N. A. Rayner (2013), EN4: Quality controlled ocean temperature and salinity profiles and monthly objective analyses with uncertainty estimates, Journal of Geophysical Research: Oceans, 118(12), 6704-6716, doi:10.1002/2013JC009067.

Gordon, A. L., and C. F. Giulivi (2014), Ocean eddy freshwater flux convergence into the North Atlantic subtropics, 119(6), 3327-3335, doi:10.1002/2013JC009596.

Gordon, A. L., C. F. Giulivi, J. Busecke, and F. M. Bingham (2015), Differences among subtropical surface salinity patterns, Oceanography, 28(1), 32–39, doi:10.5670/oceanog.2015.02.

Gruenberg, L. K. (2021), Indonesian Throughflow Heat Transport, and Spreading within the Eastern Tropical Indian Ocean, PhD dissertation, Columbia University, doi:10.7916/d8-s7eg-ke09.

Gu, D., and S. G. Philander (1997), Interdecadal climate fluctuations that depend on exchanges between the tropics and extratropics, Science, 275(5301), 805-807.

576 Han, W., and J. P. McCreary Jr (2001), Modeling salinity distributions in the Indian Ocean,
577 Journal of Geophysical Research: Oceans, 106(C1), 859-877,
578 doi:10.1029/2000JC000316.

579 Holte, J., and L. Talley (2009), A New Algorithm for Finding Mixed Layer Depths with
580 Applications to Argo Data and Subantarctic Mode Water Formation*, Journal of
581 Atmospheric and Oceanic Technology, 26(9), 1920-1939,
582 doi:10.1175/2009JTECHO543.1.

583 Hosoda, S., T. Suga, N. Shikama, and K. Mizuno (2009), Global Surface Layer Salinity Change
584 Detected by Argo and Its Implication for Hydrological Cycle Intensification, J.
585 Oceanogr., 65, 579-579-586, doi:10.1007/s10872-009-0049-1.

586 Johnson, B. K., F. O. Bryan, S. A. Grodsky, and J. A. Carton (2016), Climatological Annual
587 Cycle of the Salinity Budgets of the Subtropical Maxima, Journal of Physical
588 Oceanography, 46(10), 2981-2994, doi:10.1175/JPO-D-15-0202.1.

589 Kalnay, E., et al. (1996), The NCEP/NCAR 40-Year Reanalysis Project, Bulletin of the
590 American Meteorological Society, 77(3), 437-471, doi:10.1175/1520-
591 0477(1996)077<0437:TNYRP>2.0.CO;2.

592 Katsura, S., E. Oka, B. Qiu, and N. Schneider (2013), Formation and Subduction of North
593 Pacific Tropical Water and Their Interannual Variability, Journal of Physical
594 Oceanography, 43(11), 2400-2415, doi:10.1175/JPO-D-13-031.1.

595 Kessler, W. S. (1999), Interannual Variability of the Subsurface High Salinity Tongue South of
596 the Equator at 165°E*, Journal of Physical Oceanography, 29(8), 2038-2049,
597 doi:10.1175/1520-0485(1999)029<2038:IVOTSH>2.0.CO;2.

598 Kolodziejczyk, N., and F. Gaillard (2012), Observation of spiciness interannual variability in the
599 Pacific pycnocline, Journal of Geophysical Research: Oceans (1978–2012), 117(C12),
600 doi:10.1029/2012JC008365.

601 Lagerloef, G. S., et al. (2008), The Aquarius/SAC-D Mission: Designed to Meet the Salinity
602 Remote-sensing Challenge, Oceanography, 20(1), 68-81.

603 Lindstrom, E., F. Bryan, and R. Schmitt (2015), SPURS: Salinity Processes in the Upper-ocean
604 Regional Study, Oceanography, 28(1), 14, doi:10.5670/oceanog.2015.01.

605 Maes, C., N. Grima, B. Blanke, E. Martinez, T. Paviet-Salomon, and T. Huck (2018), A Surface
606 “Superconvergence” Pathway Connecting the South Indian Ocean to the Subtropical
607 South Pacific Gyre, Geophysical Research Letters, 45(4), 1915-1922,
608 doi:10.1002/2017GL076366.

609 McCreary, J., and P. Lu (1994), On the Interaction between the Subtropical and Equatorial
610 Ocean Circulations: The Subtropical Cell, Journal of Physical Oceanography, 24, 466-
611 497.

612 Menezes, V. V., H. E. Phillips, A. Schiller, N. L. Bindoff, C. M. Domingues, and M. L. Vianna
613 (2014), South Indian Countercurrent and associated fronts, Journal of Geophysical
614 Research: Oceans, 119(10), 6763-6791, doi:10.1002/2014JC010076.

615 Menezes, V. V., H. E. Phillips, A. Schiller, C. M. Domingues, and N. L. Bindoff (2013), Salinity
616 dominance on the Indian Ocean Eastern Gyral current, Geophysical Research Letters,
617 40(21), 5716-5721, doi:10.1002/2013GL057887.

618 Menezes, V. V., H. E. Phillips, M. L. Vianna, and N. L. Bindoff (2016), Interannual variability
619 of the South Indian Countercurrent, Journal of Geophysical Research: Oceans, 121(5),
620 3465-3487, doi:10.1002/2015JC011417.

621 Molinari, R. L., D. Olson, and G. Reverdin (1990), Surface current distributions in the tropical
622 Indian Ocean derived from compilations of surface buoy trajectories, Journal of
623 Geophysical Research: Oceans, 95(C5), 7217-7238, doi:10.1029/JC095iC05p07217.

624 Momin, I. M., A. K. Mitra, S. Prakash, D. K. Mahapatra, A. Gera, and E. N. Rajagopal (2015),
625 Variability of sea surface salinity in the tropical Indian Ocean as inferred from Aquarius
626 and in situ data sets, International Journal of Remote Sensing, 36(7), 1907-1920,
627 doi:10.1080/01431161.2015.1030045.

628 Nonaka, M., and H. Sasaki (2007), Formation mechanism for isopycnal temperature-salinity
629 anomalies propagating from the eastern South Pacific to the equatorial region, Journal of
630 Climate, 20(7), 1305-1315, doi:10.1175/JCLI4065.1.

631 Palastanga, V., P. J. van Leeuwen, M. W. Schouten, and W. P. M. de Ruijter (2007), Flow
632 structure and variability in the subtropical Indian Ocean: Instability of the South Indian
633 Ocean Countercurrent, Journal of Geophysical Research: Oceans, 112(C1),
634 doi:10.1029/2005JC003395.

635 Peng, S., Y.-K. Qian, R. Lumpkin, Y. Du, D. Wang, and P. Li (2015), Characteristics of the
636 Near-Surface Currents in the Indian Ocean as Deduced from Satellite-Tracked Surface
637 Drifters. Part I: Pseudo-Eulerian Statistics, Journal of Physical Oceanography, 45(2),
638 441-458, doi:10.1175/JPO-D-14-0050.1.

639 Qu, T., Z. Lian, X. Nie, and Z. Wei (2019), Eddy-Induced Meridional Salt Flux and Its Impacts
640 on the Sea Surface Salinity Maxima in the Southern Subtropical Oceans, Geophysical
641 Research Letters, 46(20), 11292-11300, doi:10.1029/2019GL084807.

642 Reid, J. L. (2003), On the total geostrophic circulation of the Indian Ocean: flow patterns,
643 tracers, and transports, Progress in Oceanography, 56(1), 137-186, doi:10.1016/S0079-
644 6611(02)00141-6.

645 Roemmich, D., and J. Gilson (2009), The 2004–2008 mean and annual cycle of temperature,
646 salinity, and steric height in the global ocean from the Argo Program, Progress in
647 Oceanography, 82, 81, doi:10.1016/j.pocean.2009.1003.1004.

648 Schanze, J. J., R. W. Schmitt, and L. L. Yu (2010), The global oceanic freshwater cycle: A state-
649 of-the-art quantification, Journal of Marine Research, 68(3-1), 569-595,
650 doi:10.1357/002224010794657164.

651 Schmidtko, S., G. C. Johnson, and J. M. Lyman (2013), MIMOC: A global monthly isopycnal
652 upper-ocean climatology with mixed layers, Journal of Geophysical Research Oceans,
653 118(4), 1658-1672, doi:10.1002/jgrc.20122.

654 Schmitt, R. W., and A. Blair (2015), A river of salt, Oceanography, 28(1), 40-45,
655 doi:10.5670/oceanog.2015.04.

Schott, F. A., M. Dengler, and R. Schoenefeldt (2002), The shallow overturning circulation of the Indian Ocean, Progress in Oceanography, 53(1), 57-103, doi:10.1016/S0079-6611(02)00039-3.

Schott, F. A., S.-P. Xie, and J. P. McCreary Jr (2009), Indian Ocean circulation and climate variability, Reviews of Geophysics, 47(1), doi:https://doi.org/10.1029/2007RG000245.

Siedler, G., M. Rouault, and J. R. E. Lutjeharms (2006), Structure and origin of the subtropical South Indian Ocean Countercurrent, Geophysical Research Letters, 33(24), doi:10.1029/2006GL027399.

Skofronick-Jackson, G., et al. (2017), The Global Precipitation Measurement (GPM) Mission for Science and Society, Bulletin of the American Meteorological Society, 98(8), 1679-1695, doi:10.1175/BAMS-D-15-00306.1.

Stramma, L., and J. R. E. Lutjeharms (1997), The flow field of the subtropical gyre of the South Indian Ocean, Journal of Geophysical Research: Oceans, 102(C3), 5513-5530, doi:10.1029/96JC03455.

Terray, L., L. Corre, S. Cravatte, T. Delcroix, G. Reverdin, and A. Ribes (2012), Near-Surface Salinity as Nature's Rain Gauge to Detect Human Influence on the Tropical Water Cycle, Journal of Climate, 25(3), 958-977, doi:10.1175/JCLI-D-10-05025.1.

Vinogradova, N., et al. (2019), Satellite Salinity Observing System: Recent Discoveries and the Way Forward, Frontiers in Marine Science, 6, 243, doi:10.3389/fmars.2019.00243.

Wang, Y., Y. Li, and C. Wei (2020), Subtropical sea surface salinity maxima in the South Indian Ocean, Journal of Oceanology and Limnology, 38(1), 16-29, doi:10.1007/s00343-019-8251-5.

Worthington, L. (1976), On the North Atlantic Circulation, The Johns Hopkins Oceanographic Studies, 6, 110.

Yu, L., S. A. Josey, F. M. Bingham, and T. Lee (2020), Intensification of the global water cycle and evidence from ocean salinity: a synthesis review, Annals of the New York Academy of Sciences, 1472(1), 76-94, doi:10.1111/nyas.14354.

Zhang, L., and T. Qu (2014), Low-frequency variability of South Pacific Tropical Water from Argo, Geophysical Research Letters, 41(7), 2441–2446, doi:10.1002/2014GL059490.